PAPER

High Temperature Melting Curve of Basaltic Glass by Laser Flash Heating

Chin. Phys. Lett. **39**, 020701 (2022)

High Temperature Melting Curve of Basaltic Glass by Laser Flash Heating

Yukai Zhuang(庄毓凯)[1,2], Junwei Li(李俊威)[2], Wenhua Lu(卢文华)[3], Xueping Yang(杨雪萍)[3], Zhixue Du(杜治学)[3,4*], and Qingyang Hu(胡清扬)[2,4*]

[1]*Institute of Atomic and Molecular Physics, Sichuan University, Chengdu 610065, China*
[2]*Center for High Pressure Science and Technology Advanced Research (HPSTAR), Beijing 100094, China*
[3]*State Key Laboratory of Isotope Geochemistry, Guangzhou Institute of Geochemistry, Chinese Academy of Sciences, Guangzhou 510640, China*
[4]*Center for Excellence in Deep Earth Science, Guangzhou Institute of Geochemistry, Chinese Academy of Sciences, Guangzhou 510640, China*

(Received 24 November 2021; accepted 12 January 2022; published online 29 January 2022)

Basalt is an igneous rock originating from the cooling and solidification of magma and covers approximately 70% of Earth's surface. Basaltic glass melting in the deep Earth is a fundamental subject of research for understanding geophysics, geochemistry, and geodynamic processes. In this study, we design a laser flash heating system using two-dimensional, four-color multi-wavelength imaging radiometry to measure the basaltic glass melting temperature under high pressure conditions in diamond anvil cells. Our experiment not only determines the temperature at the center of heating but also constructs a temperature distribution map for the surface heating area, and enables us to assess the temperature gradient. Through precise temperature measurements, we observe that the basaltic glass melting temperature is higher than those in previous reports, which is near the normal upper-mantle isotherm, approaching the hot geotherm. This suggests that basalt should not melt in most of the normal upper mantle and the basaltic melts could exist in some hot regions.

DOI: 10.1088/0256-307X/39/2/020701

The high-pressure melting behavior of the subducted mid-ocean ridge basalt (MORB) has important implications in research of mineral chemical reaction, density profile, and rheology of Earth's deep interiors.[1] Accurate melting temperature measurements of the basaltic glass are critical for examining evolution and segregation between the surface and its interior in Earth's early history.

Over decades, different methods have been exploited to measure melting pressures of basalt at high pressure, such as the floating diamond method[2] and the multi-anvil apparatus.[1,3] Those methods were used to measure the high-pressure melting temperature below 25 GPa, which is equivalent to the depth at the top of the lower mantle. For deeper depths, the laser-heated diamond anvil cell (LHDAC) technique is more common because of its more expansive pressure-temperature (P–T) coverage compared to that of the above-mentioned methods. LHDAC is a powerful tool for simulating high-pressure (a few megabar) and high-temperature (thousands of K) conditions on materials, which enables the measurement of physicochemical properties under extreme environments.[4,5] Andrault *et al.* found that the solidus and liquidus melting temperatures of basalt were 3800 ± 300 K and 5050 ± 300 K at 135 GPa, respectively.[6] Pradhan *et al.* suggested that the solidus temperature of basalt is 3970 ± 150 K at the same pressure and thus partial melting compositions can be gravitationally stable at Earth's core-mantle boundary.[7] Tateno *et al.* determined the melting temperature of basalt to be 3700 K at 72 GPa and 4300 K at 135 GPa.[8] They observed that davemaoite and silica are the first and second liquidus phases above megabar pressures.[9] Despite these earlier studies, the melting temperature of basalt under high pressure remains controversial due to the large uncertainties of measured temperatures, which hinders us from understanding the mineralogy of the Earth.

Accurate interpretation of data obtained from LH-DAC requires high-quality calibration of not only the temperature at the center hotspot but also the associated temperature gradient, which is essentially the root cause of the aforementioned controversies.[10] During laser heating, temperature gradients can reach as large as approximately 10^2 K/μm spreading along both the axial and transverse directions on the sample. In this study, we define the axial direction as light passing through the optical window and it is usually followed by the incoming laser beam. Along the transverse direction we signify a temperature gradient on the sample surface area. In general, temperature

*Corresponding authors. Email: qingyang.hu@hpstar.ac.cn; duzhixue@gig.ac.cn

gradients become more substantial at higher temperatures. The presence of temperature gradients results from various types of imaging aberrations. For example, chromatic aberrations that may have a spectral signature[11,12] may significantly obscure the accuracy of the obtained temperature. Thus, to properly interpret measurements of physicochemical properties of samples under *in situ* high pressure and temperature conditions, it is necessary to reduce temperature gradients and visualize the temperature profile quantity of the sample during *in situ* heating.

In order to measure the high-pressure melting temperature, we must establish a robust system with high-quality heating and a minimal temperature gradient. The temperature gradients along the axial direction in LHDAC can be reduced by double-sided laser heating.[13–15] It is also possible to quantify temperature gradients along the transversal directions through the aperture, narrow-slit, or wide-slit methods.[10] All the above-mentioned methods require an emitted radiation of a hotspot from the laser-heated sample, which can be fitted to Planck's black-body radiation equation as a function of wavelength such that the temperature can be calculated accordingly.

The aperture and narrow-slit methods may be affected by diffraction due to the presence of an aperture when the operator measures the temperature from the hotspot. Large numerical errors may stem from a chromatic signature induced by diffraction.[16] Systematic errors can be produced through possible small misalignments unless the aperture is perfectly centered on the hotspot. The wide-slit method requires a spatial transformation to reconstruct the two-dimensional hotspot profile from a single spatial dimension collected by the imaging spectrometer.[10]

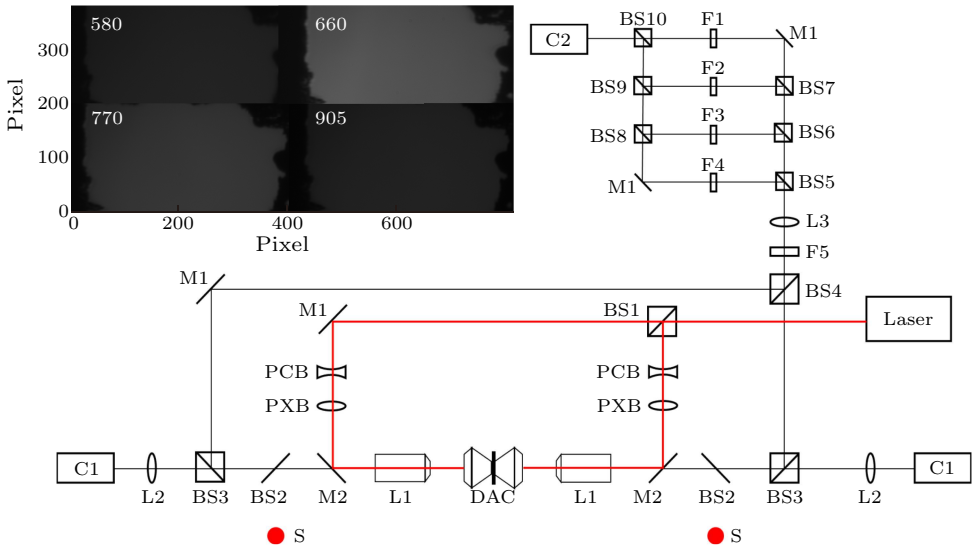

Fig. 1. Double-sided laser heating layout with four-color multispectral imaging radiometry. The top left illustration shows the raw response data for the four-color system. DAC: diamond anvil cell; Laser: SPI 300W air-cooled fiber laser; S: the white light source; L1: Mitutoyo NIR 5X Objectives; L2: Thorlabs AC254-200-B Achromat NIR lens 200 mm; L3: Thorlabs AC508-750-B Achromat NIR lens 750 mm; PCB: achromat concave lens; PXB: achromat convex lens; F1: 905 nm narrow-band filter; F2: 770 nm narrow-band filter; F3: 660 nm narrow-band filter; F4: 580 nm narrow-band filter; F5: 1064 nm narrow-band filter; M1: Thorlabs PF10-03-P01 silver mirrors; M2: laser mirrors; BS1: cube beam splitters; BS2: Thorlabs BP145B1 Pellicle beam splitter (removed during heating and calibration); BS3: OptoSigma 039–0265 cube beam splitters; BS4-10: OptoSigma 039–0260 cube beam splitters; C1: Thorlabs DCC1645C CMOS camera. C2: SBIG ST-402ME.

Strategy for Accurate Temperature Measurement with a Newly Designed Laser-Heating System. We measured two-dimensional temperature gradients using four-color multi-wavelength imaging radiometry.[17] This technique can substantially reduce the chromatic aberrations that occur in previous temperature measurements and yield a measure of emissivity of the sample. In contrast to prolonged heating, the flash heating technique (triggered by the function generator for approximately 20 ms) can effectively reduce the likelihood of chemical reaction, sample instability, and thermal runaway.[18] The optical schematic of the double-sided laser heating system is shown in Fig. 1. Although it was modified based on an available system from literature,[10,17,19] our design has made the following critical improvements. Firstly, we used a single laser and single four-color multispectral imaging radiometry spectrometer to realize double-sided heating with precise temperature measurement; such laser power can be coherently synchronized. Secondly, we introduced a certain level of portability in this system, providing the potential

for mobility. Finally, we used a fiber laser (model SPI 300W air-cooled) to allow remote control of the laser output and to eliminate mechanical vibration, which will influence the temperature gradient.

The initial laser beam (a flat laser flash pulse at 1064 nm and subsequent quick rise time of approximately 1 ms) was split into two beams and then focused onto the sample inside the diamond anvil cell (DAC) using a Mitutoyo NIR 5X objective lens L1, which is optimized for near-infrared spectroscopy and has a working distance of 37.5 mm. An achromat concave lens (PCB) and an achromat convex lens (PXB) were used to eliminate the possible unnecessarily small laser-heated spot using only L1[20] and to adjust the laser spot size by changing the distance between the PCB and PXB. The IR laser was partially absorbed by the sample in the DAC, and the sample emitted thermal radiation as a function of temperature via Planck's law:

$$I(\lambda,T)=2\mathcal{E}(\lambda,T)\pi hc^2\lambda^{-5}\left[\exp\left(\frac{hc}{\lambda kT}-1\right)\right]^{-1}, \quad (1)$$

where I is the spectral intensity, $\mathcal{E}$ is the emissivity, λ is the wavelength, T is the temperature, h is Planck's constant, c is the speed of light, and k is Boltzmann's constant.

The thermal emission was split into four wavelengths on each side using four narrow-band filters (F1–F4). Then, the eight images from the two sides were simultaneously received by a thermo-electrically cooled charge-coupled device (CCD) (C2: SBIG ST-402ME). Next, the images were spatially registered to produce two-dimensional temperature maps and relative emissivity after correction for the relative response and background of each image.

A standard coil lamp with a maximum power of 45 W was used to calibrate the optical response of the system for each of the eight wavelength bands. The $I(\lambda)$ of the lamp complied with NIST standards (Newport Corp. 63358). To project all well-separated images onto the CCD camera, the lamp was placed behind a 150 μm pinhole in the focal plane of L1, and the entire four-color optical system (from BS5 to C2) was enclosed in a black box. The influence of the distance between the lamp and pinhole on the calibrated results was minor. The main focus was to guarantee that the eight images were correctly recognized without overlapping on the CCD camera, such that their central portions were free of diffraction edge effects.[17]

Temperature Measurement. An intensity measurement for the eight images and an accurate registration to each other were required for the temperature determination of thermal emission in the LHDAC. The images were registered using the image correlation methods with linear interpolation to achieve a coincidence within 0.2 pixels (approximately 0.1 μm). The correlation coefficient R is expressed as

$$R=\frac{\sum_{i=1}^{n}(X_i-\bar{X})(Y_i-\bar{Y})}{\sqrt{\sum_{i=1}^{n}(X_i-\bar{X})^2}\sqrt{\sum_{i=1}^{n}(Y_i-\bar{Y})^2}}, \quad (2)$$

where X is the intensity, and Y is the shape. If the correlated images are perfect, then $R=1$. If the images are not correlated, then $R=0$. Typically, R is greater than 0.99 with a debugged system.

After correcting the intensity and establishing the spatial correlation for the eight images, we fit a set of pixel-by-pixel spectra using the Wien function provided by the intensities in each image:

$$\text{Wien}=\frac{k}{hc}\ln\left[\frac{2\pi hc^2}{I\lambda^5}\right], \quad (3)$$

which can be simplified (as the system has only four wavelength bands) by:

$$\text{Wien}\approx\frac{1}{\lambda}\frac{1}{T}-\frac{k}{hc}\ln\mathcal{E}, \quad (4)$$

where k is Boltzmann's constant, h is Plank's constant, c is the speed of light, and $\mathcal{E}$ is the emissivity. The temperature can then be obtained using the slope of a weighted linear least-squares fit. We assumed that the sample emissivity was independent of the wavelength (λ), and the intensities of the images were fitted to two adjustable parameters: temperature and gray-body emissivity (gray-body approximation). If the temperature determination of the optical system is based on full spectra rather than only four wavelength bands, the approximation is no longer statistically supported. The calculated uncertainty is generally less than 5% using the gray-body Wien approximation and is negligible below 4000 K compared to that of the Planck fit.[21] Other system errors can include calibrations, corrections, or differences between multiple measurements (<2%).

Table 1. The compositions of the basalt melt in units of wt%. The numbers in parenthesis are uncertainties.

Composition	Content (wt%)
K_2O	0.018(2)
CaO	11.13(5)
Na_2O	0.12(1)
MgO	12.59(24)
Al_2O_3	15.27(13)
SiO_2	50.97(21)
FeO	8.62(16)
Others	1.27(12)
Total	100.00

MORB Melting. We used the laser heating system to measure the MORB melting temperatures at different pressures (Fig. 2). Before loading the MORB sample, the chemical composition was determined by electron probe micro analysis (EPMA), as listed in Table 1. The compositions of the samples were similar

to those reported in previous studies.[2,3] The sample was then loaded into a 100-μm sample chamber of a 300-μm DAC to achieve high-pressure and high-temperature conditions. The pressure was determined using the ruby R_1 emission line.[22] The sample was then heated at 10.8, 20.6, 25.6, and 37.2 GPa, respectively.

The samples were viewed with C2 and both of C1 during the laser heating measurements. The laser power was increased until the thermal emission of the basalt glass reached the desired level (but not saturation), such that the image frame in the CCD detector (C2) was clear enough for capturing. Similar to the representative data images shown in Fig. 2, the laser heating spots were recorded at both sides simultaneously and separated into each of the four wavelengths. The spot was approximately 50–60 μm in diameter, but not perfectly symmetrical. The temperature gradient was calculated visually in the laser-heated spot. Among the black curves for the melt area, the temperature was not homogeneous. Generally, the temperature distribution was measured from the center of the spot at 3200 K down to the edge of the spot at 2900 K on one side and 3000 to 2700 K on the other side.

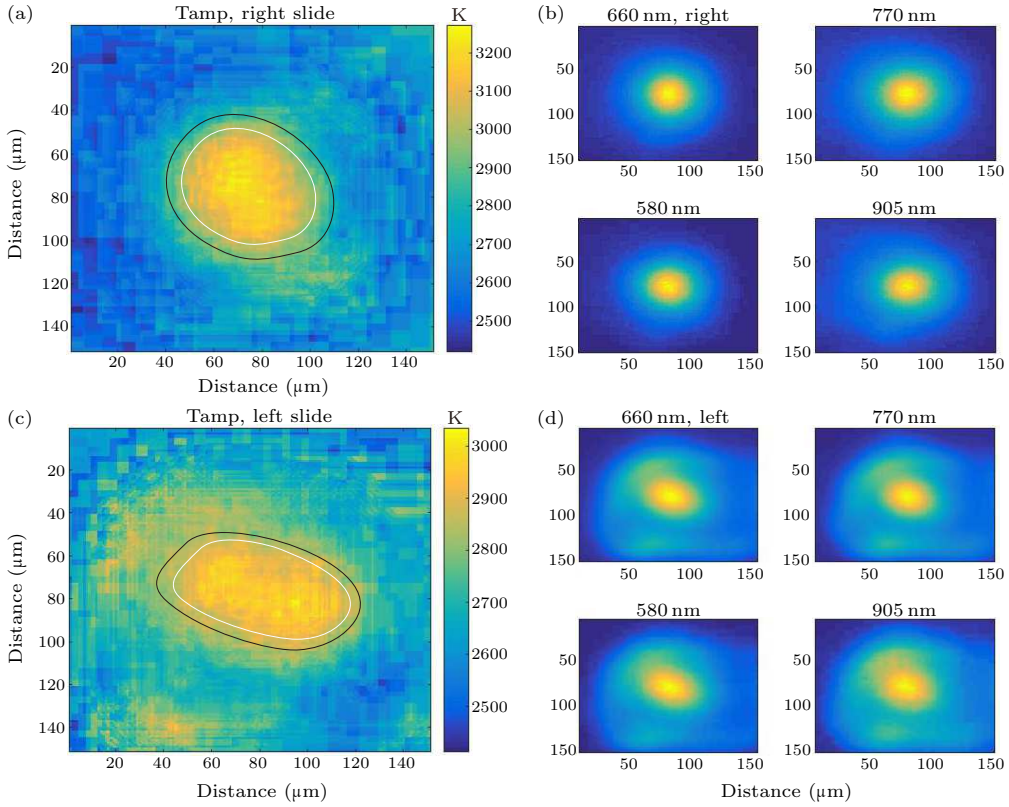

Fig. 2. The two-dimensional temperature maps based on the four-color method in the laser heating progress. (a) and (c) The calculated temperature maps of the right side and left side of the heating sample, respectively. The two black curves are the guide curves showing the laser spots, and the two white curves represent the melting area. (b) and (d) The four obtained wavelengths (580, 660, 770, and 905 nm) from the laser-heated spot of the right side and left side, respectively.

The image shown in Fig. 2 represents the melting. The obtained temperature at the center of the heating exceeded the melting temperature of the basalt. An accurate melting temperature is obtained by an abrupt transition in the temperature-emissivity map across the laser heating spot (Fig. 3).[20] The emissivity points versus temperature were obtained from the pixels across a vertical transect of the heating spot, as shown in Fig. 2. The emissivity will climb with temperature before melting and remain on a downswing upon melting. The shape of the temperature gradient outside the laser spot was irregular in areas affected by the scattering light from the thermal emission of the laser spot. We heated the sample at different pressures before decompressing it to the ambient pressure (inset in Fig. 4). The optical image showed that the laser heated spot displayed a concentric texture, in which an opaque circle located at the center of the spot was surrounded by a transparent portion. The opaque pools reflected the melt area of the sample (hottest at the center). The transparent portion represents the liquidus phase that dissolved at the spot center and then precipitated at the liquidus temperature due to saturation gradient chemical diffusion.[9]

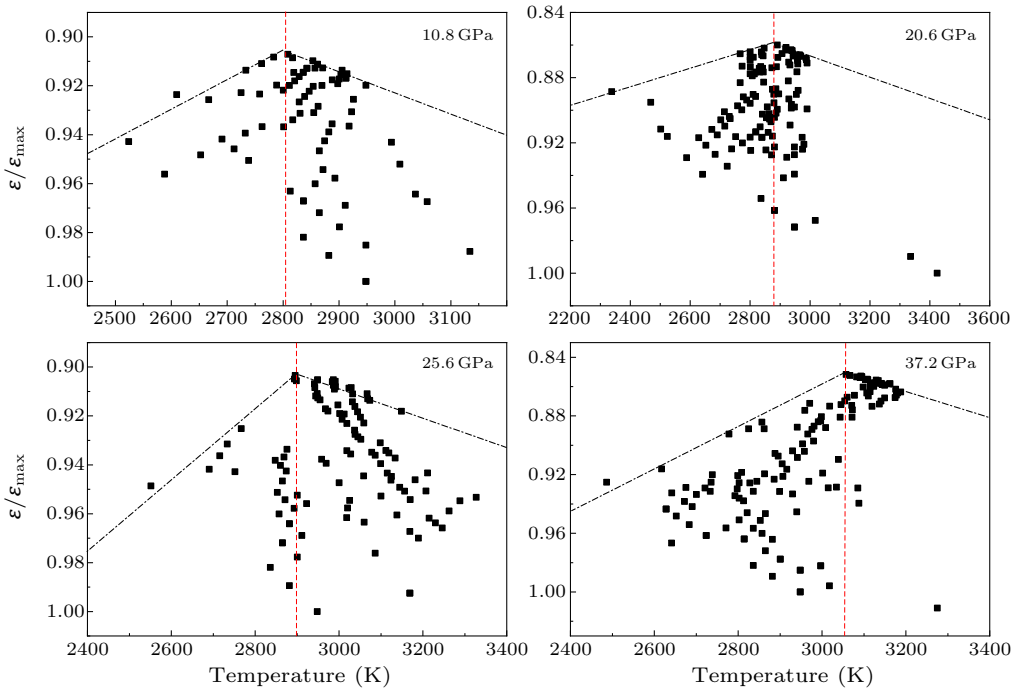

Fig. 3. The emissivity $\mathcal{E}$ versus temperature for a vertical transect across the center of the basalt hot spot in Fig. 2. The red line in each subfigure shows the discrepancy in the emissivity maps, which is associated with the melting temperature. The black dot-dashed lines are guide of the eyes for the discrepancy.

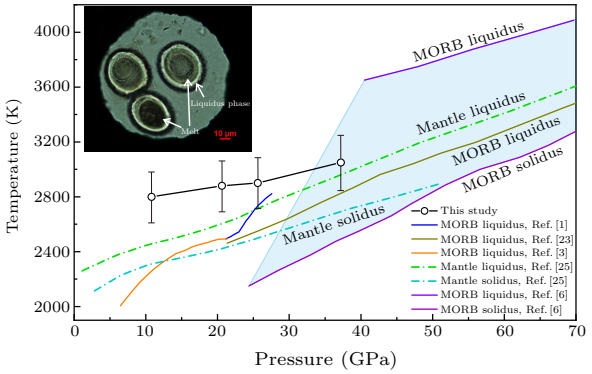

Fig. 4. The basalt melting temperature curve in this study is compared with other curves of the MORB and mantle.[1,3,6,23–25] The inserted optical image of basalt was obtained after flash laser heating and decompression. Opaque melt areas were formed at the center of the laser-heated spot surrounded by the transparent liquidus phase.

Figure 3 shows that the melting temperature of the basalt was approximately 2800 ± 190 K at 10.8 GPa, 2880 ± 200 K at 20.6 GPa, 2910 ± 200 K at 25.6 GPa, and 3050 ± 210 K at 37.2 GPa, which represents liquidus temperature. The obtained basalt melting temperatures were higher than those of Hirose *et al.*,[23] lower than those of Andrault *et al.*[6] using DAC, and closest to the experiment of Hirose *et al.*[1] using a multi-anvil press (MAP) (Fig. 4). Our results were 200 to 400 K higher than that of the MAP experiment, which may be due to the minor difference in the composition proportion of the sample, the effects from the absolute values obtained by the absorption coefficients, and the differences in the wavelength-dependent absorption that were parameterized in the Wien approximation.[24] Compared our results using DAC and the previous results,[1] the MORB melting temperatures are further constrained to be higher than the mantle liquidus temperature in the upper part of the lower mantle (25–37 GPa). The subducted basalt should not melt at such depths,[25] except in some hot spot areas such as the Archean mantle plumes, in which the temperatures are 300 to 400 K higher than the temperature of the uppermost lower mantle average geotherm.[26] The MORB could melt in these areas and participate in crustal recycling. In addition to those hot spot regions, the MORB will continue to subduct deeper.[27] Our results support that the subdued MORB may reach the lowermost mantle and melt to create anomalies at the core-mantle boundary. The subducted basaltic melt could accumulate at the lowest mantle due to gravitational stability,[2] which can explain the ultralow-velocity zones (ULVZs) in Earth's core-mantle boundary regions.[28]

In conclusion, we have established a powerful, affordable double-sided laser heating system for *in situ* two-dimensional (2D) temperature measurements using the four-color method that was based on multi-wavelength imaging radiometry. Upon completing this system, we created high-quality 2D temperature maps using flash heating on both sides of the basalt sample in LHDAC and resolved temperature gradient to derive melting temperatures. Our results show that basalt melts above the average mantle isotherm

in the upper part of the lower mantle. The basaltic melt may subduct and accumulate at the lowest mantle and generate a sharp seismic velocity reduction to be observed on the surface.

Acknowledgments. This work was financially supported by the National Natural Science Foundation of China (Grant Nos. 42150101 and U1530402) and the CAEP Research Project (Grant No. CX20210048). Y.Z. is supported by the China Postdoctoral Science Foundation (Grant No. 18NZ021-0213-216308). Q.H. is supported by the Tencent Xplorer Prize. Z.D. thanks the funding support from Chinese Academy of Sciences and State Key Laboratory of Isotope Geochemistry (Grant Nos. 29Y93301701 and 51Y8340107) and the Strategic Priority Research Program (B) (Grant No. XDB18030604).

References

[1] Hirose K and Fei Y 2002 *Geochim. Cosmochim. Acta* **66** 2099
[2] Ohtani E and Maeda M 2001 *Earth Planet. Sci. Lett.* **193** 69
[3] Yasuda A, Fujii T and Kurita K 1994 *J. Geophys. Res. Solid Earth* **99** 9401
[4] Yoo C S 2020 *Matter Radiat. Extrem.* **5** 018202
[5] Hu Q and Mao H K 2021 *Matter Radiat. Extrem.* **6** 068101
[6] Andrault D, Pesce G, Bouhifd M A, Bolfan-Casanova N, Henot J M and Mezouar M 2014 *Science* **344** 892
[7] Pradhan G K, Fiquet G, Siebert J, Auzende A L, Morard G, Antonangeli D and Garbarino G 2015 *Earth Planet. Sci. Lett.* **431** 247
[8] Tschauner O, Huang S, Yang S, Humayun M, Liu W, Gilbert C S N, Bechtel H A, Tischler J and Rossman G R 2021 *Science* **374** 891
[9] Tateno S, Hirose K, Sakata S, Yonemitsu K, Ozawa H, Hirata T, Hirao N and Ohishi Y 2018 *J. Geophys. Res. Solid Earth* **123** 5515
[10] Kavner A and Nugent C 2008 *Rev. Sci. Instrum.* **79** 024902
[11] Boehler R and Chopelas A 1991 *Geophys. Res. Lett.* **18** 1147
[12] Benedetti L R, Guignot N and Farber D L 2007 *J. Appl. Phys.* **101** 013109
[13] Shen G, Rivers M L, Wang Y and Sutton S R 2001 *Rev. Sci. Instrum.* **72** 1273
[14] Watanuki T, Shimomura O, Yagi T, Kondo T and Isshiki M 2001 *Rev. Sci. Instrum.* **72** 1289
[15] Zhou Q, Ma Y, Cui Q, Cui T, Zhang J, Xie Y, Yang K and Zou G 2004 *Rev. Sci. Instrum.* **75** 2432
[16] Jeanloz R and Kavner A 1996 *Phil. Trans. R. Soc. Lond. A* **354** 1279
[17] Du Z, Amulele G, Benedetti L R and Lee K K 2013 *Rev. Sci. Instrum.* **84** 075111
[18] Yang L, Karandikar A and Boehler R 2012 *Rev. Sci. Instrum.* **83** 063905
[19] Kupenko I, Dubrovinsky L, Dubrovinskaia N, McCammon C, Glazyrin K, Bykova E, Boffa B T, Sinmyo R, Chumakov A I, Potapkin V, Kantor A, Ruffer R, Hanfland M, Crichton W and Merlini M 2012 *Rev. Sci. Instrum.* **83** 124501
[20] Campbell A J 2008 *Rev. Sci. Instrum.* **79** 015108
[21] Benedetti L R and Loubeyre P 2007 *High Press. Res.* **24** 423
[22] Mao H K, Xu J and Bell P M 1986 *J. Geophys. Res. Solid Earth* **91** 4673
[23] Hirose K, Fei Y W, Ma Y Z and Mao H K 1999 *Nature* **397** 53
[24] Deng J, Du Z, Benedetti L R and Lee K K 2017 *J. Appl. Phys.* **121** 025901
[25] Andrault D, Bolfan-Casanova N, Nigro G L, Bouhifd M A, Garbarino G and Mezouar M 2011 *Earth Planet. Sci. Lett.* **304** 251
[26] Herzberg C 1995 *Chem. Geol.* **126** 1
[27] Zhuang Y, Gan B, Cui Z, Tang R, Tao R, Hou M, Jiang G, Popescu C, Garbarino G, Zhang Y and Hu Q 2021 *Sci. Bull.* (in press)
[28] Liu J, Hu Q, Kim D Y, Wu Z, Wang W, Xiao Y, Chow P, Meng Y, Prakapenka V B, Mao H K and Mao W L 2017 *Nature* **551** 494